In situ conformational changes of the *Escherichia coli* serine chemoreceptor in different signaling states

Wen Yang[1], C. Keith Cassidy[2,3], Peter Ames[4], Christoph A.Diebolder[5], Klaus Schulten[3], Zaida Luthey-Schulten[6], John S. Parkinson[4] and Ariane Briegel[1,*]

1. Institute of Biology, Leiden University, Leiden, The Netherlands
2. Department of Biochemistry, University of Oxford, Oxford OX1 3QU, UK
3. Department of Physics and Beckman Institute, University of Illinois Urbana-Champaign, Urbana, IL, USA
4. School of Biological Sciences, University of Utah, Salt Lake City, UT, USA
5. NeCEN, Leiden University, Leiden, The Netherlands
6. Department of Chemistry and Center for the Physics of Living Cells, University of Illinois Urbana-Champaign, Urbana, IL, USA

*For Correspondence:
Ariane Briegel
Institute of Biology, Leiden University, Sylviusweg 72, 2333 BE Leiden, The Netherlands
Phone: +31 (71) 527 8850 17
Email: a.briegel@biology.leidenuniv.nl

Abstract

Tsr, the serine chemoreceptor in *Escherichia coli*, transduces signals from a periplasmic ligand-binding site to its cytoplasmic tip, where it controls the activity of the CheA kinase. To function, Tsr forms trimers-of-homodimers (TODs), which associate *in vivo* with the CheA kinase and CheW coupling protein. Together, these proteins assemble into extended hexagonal arrays. Here, we use cryo-electron tomography (cryoET) and molecular dynamics simulation to study Tsr in the context of a near-native array, characterizing its signaling-related conformational changes at both the individual dimer and the trimer level. In particular, we show that individual Tsr dimers within a trimer exhibit asymmetric flexibilities that are a function of the signaling state, highlighting the effect of their different protein interactions at the receptor tips. We further reveal that the dimer compactness of the Tsr trimer changes between signaling states, transitioning at the glycine hinge from a compact conformation in the kinase-OFF state to an expanded conformation in the kinase-ON state. Hence, our results support a crucial role for the glycine hinge: to allow the receptor flexibility necessary to achieve different signaling states while also maintaining structural constraints imposed by the membrane and extended array architecture.

Importance

In *Escherichia coli*, membrane-bound chemoreceptors, the histidine kinase CheA, and coupling protein CheW form highly-ordered chemosensory arrays. In core signaling complexes, chemoreceptor trimers-of-dimers undergo conformational changes, induced by ligand binding and sensory adaptation, which regulate kinase activation. Here, we characterize by cryo-electron tomography the "kinase-ON" and "kinase-OFF" conformations of the *E. coli* serine receptor in its native arrays context. We found distinctive structural differences between the members of a receptor trimer, which contact different partners in the signaling unit, and structural differences between the ON and OFF signaling complexes. Our results provide new insights into the signaling mechanism of chemoreceptor arrays and suggest an important functional role for a previously postulated flexible region and glycine hinge in the receptor molecule.

Keywords

Chemotaxis; chemoreceptor arrays; Tsr chemoreceptor;

Introduction

Most motile bacteria sense and track chemical gradients in their environment, a behavior called chemotaxis (1, 2). Chemotactic signaling has been extensively studied in the model organism *Escherichia coli* and is especially notable for its high sensitivity, signal amplification, and wide dynamic range (3-5). Transmembrane chemoreceptors bind ligands in the periplasm and relay signals across the inner membrane to modulate the autophosphorylation activity of the cytoplasmic histidine kinase CheA (6) . Attractant stimuli suppress CheA kinase activity, reducing the flux of phosphoryl groups to the cytoplasmic response regulator CheY. Phospho-CheY binds to the flagellar motor and biases its rotation from the default counter-clockwise direction to clockwise. To follow chemoeffector gradients, the chemotaxis system needs to constantly fine-tune its detection sensitivity. Sensory adaptation is made possible by two enzymes: the methyltransferase CheR, which adds methyl groups at specific glutamyl residues in the cytoplasmic portion of chemoreceptors, and the methylesterase CheB, which removes methyl groups from these same sites (7). A fully methylated receptor elicits high CheA activity ("kinase-ON"), while a fully demethylated receptor down-regulates CheA activity ("kinase-OFF") (Fig. 1A).

E. coli chemoreceptor signaling complexes assemble into extended membrane-bound arrays at the cell pole, which integrate signals from thousands of chemoreceptors through a highly ordered baseplate of CheA kinases and CheW coupling proteins. The signaling core unit comprises two receptor trimers-of-dimers (TODs), one CheA homodimer and two CheW proteins (8-10). This minimal functional unit is also the structural core unit in the array (11-13). By linking together at specific interfaces between CheA and CheW, core units form a ~12 nm spaced hexagonal array

with a receptor trimer at each vertex (Fig. 1B). This hexagonal receptor packing is not only found in *E. coli*, but is likely universal among bacteria and archaea. *E. coli* contains five different chemoreceptors (Tar, Tsr, Tap, Trg and Aer) for sensing a variety of chemicals. Due to their similar physical length and high sequence conservation at their cytoplasmic tips, all five chemoreceptors integrate into a single, continuous receptor array (9, 14-16).

Tsr, the serine receptor of *E. coli*, is a 551 amino acid protein that spans roughly 31 nm perpendicular to the membrane (12, 17). The receptor homodimers consist of three functional modules that mediate stimulus sensing, input-output control, and kinase control (Fig. 1C) (1, 3). Ligands bind to receptors either directly or indirectly via periplasmic binding proteins (PBPs) at the ligand-binding domain in the periplasm. The signal is then transmitted from the transmembrane domain to the cytoplasmic portion of the receptor through a five-residue control cable that modulates the HAMP (Histidine, Kinase, Adenylate cyclases, Methyl accepting proteins and Phosphatases) domain (18, 19). The 50-residue HAMP domain forms a parallel four-helix bundle that relays stimulus signals to the kinase control module (20, 21), a continuous anti-parallel, coiled-coil bundle with a hairpin turn at the membrane-distal end. The methylation helix bundle contains the conserved glutamyl residues that are the sites of adaptational modifications by CheR and CheB. In the flexible bundle (14), three conserved glycine residues reside in a plane transecting the coiled-coil axis termed the ‘glycine hinge’ and may enable the bundle to bend (22, 23). The hairpin tip bundle contains the interfaces through which receptor dimers form trimers as well as directly interact with CheA and CheW (14, 24-26).

Numerous studies have investigated the molecular mechanism of signal transmission in chemoreceptors. A growing body of evidence suggests that kinase activation is likely achieved through dynamic shifts of local conformational alternations in the contiguous helix regions along the receptor (2, 27). The 'dynamic-bundle model' suggests the kinase-ON output state corresponds to a dynamic, less tightly packed HAMP domain and a stably packed methylation helix (MH) bundle, while the kinase-OFF output state is characterized by a stable HAMP domain and a dynamic MH bundle (28, 29). In addition, the 'yin-yang model' provides a global view on the long-range allosteric interplay of the kinase control module. Here, the kinase-OFF output state is correlated to a loosely packed MH bundle and a tight packing of the proteins in the interaction region at the hairpin tips. In contrast, the kinase-ON output displays a tight, 'frozen' packing of the MH bundle and a looser helix packing at the tips (30). Together, these studies suggest that sensory signals are propagated along the receptor through dynamic changes in helix-bundle packing, which toggle the receptor between the kinase-ON and kinase-OFF output states. The receptor coupling to the kinase is likely assisted by one or more specific residues, which are key to the overall stability of the receptor tips as well as for kinase control through receptor-CheA and receptor-CheW interfaces (31-33).

In this study, we aimed to characterize the signaling conformational changes of Tsr in its near-native cellular context. We combined cryo-electron tomography (cryo-ET) with subtomogram averaging and molecular dynamics simulation to study Tsr in the context of *in vivo* assembled arrays. Our results show that the compactness of receptor dimers within individual receptor trimers changes with signaling state. In the kinase-ON state, receptors in trimers are more splayed than those in kinase-OFF arrays, a feature that is most distinctive around the location of

136 the glycine hinge. We thus propose that the glycine hinge imparts the flexibility necessary for
137 smooth bending in the individual receptors, as well as the changes in compactness at the trimer
138 level. Our results also revealed receptor asymmetry within the trimer that might play a critical
139 role in determining receptor conformational dynamics in the context of the higher-order array
140 lattice.

141 ## Results

142 **Improved *E. coli* strains for ECT studies**

143 To maximize homogeneity of receptor arrays, the strains used in this study contained Tsr as their
144 sole chemoreceptor. In addition, all strains lacked the adaptation enzymes CheR and CheB to
145 maintain the Tsr molecules in a uniform modification state. We imaged three Tsr modification
146 variants: Tsr [QQQQ], which mimics the fully methylated, kinase-ON state; Tsr [EEEE],
147 representing a fully unmethylated, kinase-OFF state; and wild-type Tsr [QEQE], which has an
148 intermediate modification and activity state (3).
149
150 The chemoreceptor arrays in *E. coli* are known to assemble into an ultrastable structure both *in*
151 *vivo* (34) and *in vitro* (35, 36). This feature has been exploited in previous studies, allowing *in*
152 *situ* analysis of the assembled array structure in lysed *E. coli* cells, induced either by a phage
153 lysis gene or antibiotic treatment (13, 34, 37). To increase the size and number of chemoreceptor
154 arrays, previous studies overexpressed array components from plasmids (13, 34). Although array
155 sizes increased substantially, the typical native architecture, especially of the baseplate
156 components (CheA and CheW), seemed to be compromised in such strains (13). To increase

157 array sizes in this study, we imaged strains deleted for *flgM,* in which expression of all class III
158 flagellar and chemotaxis genes is derepressed about five-fold (38).

159 **Chemoreceptor arrays maintain native architecture in lysed *E. coli***

160 Before preserving specimens by vitrification, we treated *E. coli* strains at the early exponential
161 growth phase with penicillin G to induce gentle lysis, thereby releasing cytoplasm and flattening
162 the cells. Tomograms of cell poles containing chemoreceptor arrays revealed average cell
163 thickness under 200 nm compared to unlysed *E. coli* cells that are typically more than 500 nm in
164 width (Fig. S1). The receptors retained their well-ordered hexagonal packing, consistent with
165 previous studies (13, 39). However, instead of a single array, we observed several array patches
166 of various sizes, possibly a side effect of lysis treatment on large arrays (Fig.2A-C).
167 Subtomogram averaging of the receptor hexagons yielded a 12.8 nm regular spacing for arrays in
168 all signaling states. Analysis of the tomographic images also showed that the kinase occupancy
169 at the baseplate was comparable in all strains (Fig.2 D-E). We conclude that all imaged arrays
170 have the expected native architecture.
171

172 **Core complex structure in different signaling states**

173 Subtomogram averages were obtained by receptor-based image alignments and subsequent
174 classification based on the occupancy of CheA underneath the receptor hexagons (Fig. 2D & E).
175 We found two major structural classes: receptor hexagons with three CheA dimers bound at their
176 tips and receptor hexagons lacking CheA. We calculated subtomogram averages for the three-
177 CheA hexagon class for each of the Tsr variants. The coupling protein CheW was poorly
178 resolved in all maps due to its relatively small size (18 kDa) and its preferred orientation in the
179 lysed specimens. Nevertheless, the structural information in the receptor region was only slightly

affected by the orientation preference (Fig S2). We have, therefore, focused this analysis on structural differences between receptors in different output states, in particular highlighting the EEEE and QQQQ maps. Data for Tsr _QEQE can be found in the supplementary material (Fig S3).

The QQQQ and EEEE receptor hexagon maps were similar in the region near the baseplate (Fig. 3A). In the QQQQ map, the cytoplasmic portion of the receptor from the hairpin tip to just beneath the HAMP domain was clearly visible. In contrast, the HAMP-proximal region of the receptors in the EEEE maps was less well-resolved. These results indicate higher structural stability of the receptor trimers near the baseplate in both ON and OFF output states compared to the membrane-proximal portions of the receptors.

To illustrate state-dependent conformational differences in the core units, we calculated maps for individual core complexes rather than whole hexagons. The resolutions for the core complex maps are 20 Å for QQQQ and 24Å for EEEE, which are sufficiently similar for tertiary structure comparison (Fig.S4). Alignment of the core complexes helped to improve alignment of the receptor density, especially for the EEEE map (Fig. 3B). A cross section of the core complex revealed splaying between the receptor dimers in the QQQQ map. The EEEE map also exhibited some receptor splay; however, distinct separation of the individual receptor dimers occurred farther from the hairpin tip. The density distributions of the receptor trimers also exhibited clear differences (Fig. S5).. The QQQQ maps exhibited strong receptor density extending nearly to the HAMP domain; whereas the EEEE maps exhibited weaker HAMP-proximal density, implying more structural flexibility

The CheA domains P1, P2 and P4 compose a "keel density" protruding beneath the baseplate away from the receptors (34). The size of the keel density appears to be different in the EEEE and QQQQ maps even though the individual CheA domains were not distinguishable (Fig. 3B). The volume of this keel density was 34% greater in the EEEE map than in the QQQQ map. This difference in keel size is consistent with previously reported results for core complexes with different kinase activities (34). The larger keel of CheA in the kinase-OFF state may be due, at least in part, to an unproductive immobilization of the P1 and P2 domains (40).

Structural differences of receptor trimers

The analysis of the density maps revealed structural differences not only at the core complex level, but also within the receptor trimers. Although receptor dimers interact symmetrically with one another to form a trimer, each receptor molecule also directly interacts with a different component of the base plate (Fig. 4A). Here, we use "AA" to refer to a dimer that interacts with the P5 domain of CheA, "AW" to refer to a dimer that interacts with a CheW bound to CheA•P5, and "WW" to refer to a dimer that interacts with a CheW that has no direct interaction with CheA. We note, however, that in native arrays, not all of the WW dimers may be bound to CheW (41).

The density maps revealed structural asymmetry between the different dimers in a trimer. In the kinase-ON state, the three dimers diverge from the trimer axis at more or less the same location, although the WW dimer diverges a bit closer to the baseplate. The WW dimer also displayed the weakest density of the three dimers. In the kinase-OFF state, the receptors splay farther from the

baseplate. We term this observation 'dimer zipping' (Fig. 4B) because the dimers form a strong, compact density until they splay apart. After separating from the zipped region, the WW dimer, in particular, shows a decreased density, suggesting a substantial loss of its structural rigidity near the HAMP domain.

The AW and AA dimers also exhibited structural asymmetry in different signaling states. Although a direct, quantitative comparison of the receptor densities in the QQQQ and EEEE maps is challenging, the dimers within each of the maps suggested a subtle structural difference between the AW and AA dimers. In the kinase-ON signaling state, the AA dimer appears to be the most rigid one throughout its full length. In contrast, structural rigidity of the AW dimer seems to extend closer towards the HAMP domain in the kinase-OFF state than in the kinase-ON state. Our data thus reveal signaling-dependent structural or dynamic differences between the members of a receptor trimer of dimers.

Molecular modeling of the Tsr trimer in different signaling states

To gain deeper insight into signaling-related changes in Tsr, we investigated the structural differences observed in our ECT data with molecular modeling. We first assigned atomistic structure to the receptor densities seen in our QQQQ and EEEE maps, focusing on a single receptor trimer in each state. Although individual receptor dimers could be clearly distinguished within both maps (Fig. 4), the symmetric nature of the coiled-coil bundles as well as the existence of density corresponding to CheA and CheW prevented the unambiguous docking of lone receptor dimers. Hence, to preserve the known trimer-forming interfaces between receptors during the docking procedure, we first constructed a model of the cytoplasmic portion of the Tsr

249 trimer-of-dimers (residues 259-516) based on existing crystallographic structures (17, 42), using
250 Targeted Molecular Dynamics to reproduce critical inter-receptor contacts at the side-chain level
251 (Fig. S6). Next, to extract the regions of density corresponding specifically to the receptor
252 trimers within each map, we docked an existing model of the *T. maritima* core signaling complex
253 that contains both CheA and CheW (PDB 3JA6) (41). This enabled a reliable interpretation of
254 the baseplate density and consistent positioning of our Tsr trimer model within each map. We
255 then used Molecular Dynamics Flexible Fitting (MDFF) simulations (43, 44) to refine the
256 conformational overlap between the receptor trimer model and each map. To ensure the
257 robustness of the obtained fits, a total of five MDFF simulations were conducted for each state,
258 giving rise to nearly identical conformations in each case (backbone root-mean-square deviations
259 of 1.23 +/- 0.11 Å for QQQQ and 1.70 +/- 0.10 Å for EEEE).
260
261 Visual inspection of the flexibly-fit conformations confirm that the Tsr trimer is markedly more
262 compact, on average, in the kinase-OFF state than the kinase-ON state (Fig. 5A, Mov. S1). To
263 quantify this difference, we decomposed the receptor homodimers from the EEEE and QQQQ
264 trimer models into layers based on coiled-coil packing and computed their central axis along
265 with the symmetry axis of the receptor trimer using TWISTER (Fig. 5B) (45). The layer-by-layer
266 distances between the central axis of each homodimer and the trimer axis reveal a considerable
267 inhomogeneity in the overall splay of the kinase-OFF trimer (Fig 5C). Specifically, whereas the
268 receptors diverge uniformly from the trimer axis uniformly in the kinase-ON state, remaining
269 relatively straight and interacting only at the hairpin tip, they exhibit a pronounced bend in the
270 kinase-OFF state that is centered on the glycine hinge. This bending facilitates the transition
271 from a compact trimer configuration, in which the flexible-bundle regions of the homodimers

interact, to one in which they are well separated in the methylation-helix bundle region (Mov. S1). Similarly, the comparison of the AA, AW, and WW homodimer axes between states highlights that the overall greatest change in each receptor occurs in the flexible bundle region, with the WW homodimer showing the largest difference of the three (Fig. S7). Thus, our simulations provide new molecular insight into Tsr signaling, and highlighting, in particular, the key role of glycine hinge in facilitating the transition between signaling states at the receptor trimer level.

Discussion

Signal state affects stability of the methylation-helix bundle

The present study and numerous previous ECT attempts failed to unveil the structure of full-length chemoreceptors *in situ* (11, 12, 34). Although we were not able to resolve the periplasmic, transmembrane, and HAMP regions of the receptors, we were able to clearly show signaling related conformational differences throughout the kinase control module of Tsr. A particularly distinctive difference was observed in the MH bundle, where the receptors exhibited a more continuous density distribution in the kinase-ON output state compared to the kinase-OFF. This observation agrees with the idea that receptor methylation enhances helix-packing interactions (30, 46). Thus, in our ECT results, receptor density in the MH bundle region was less prominent in the EEEE trimers, suggesting that the adaptation region is structurally more dynamic in the kinase-OFF state. It is worth mentioning that conformational heterogeneity in the kinase-OFF dataset, due to the aforementioned zipping behavior within trimers, may also contribute to the poorly resolved nature of the MH bundle in this state.

Role of the glycine hinge in signal-state switching

We suggest that the state-dependent splayed versus zipped arrangements of receptors in the flexible bundle region reflect conformational coupling between the MH bundle and the hairpin tip bundle. To our knowledge, these state-dependent structural differences have not been previously observed in imaging studies. Our MDFF analyses show that the flexible bundle region of the receptor exhibits the most dramatic structural differences between signaling states. Glycine residues, located at the center of the flexible bundle region, likely facilitate splaying in the receptor trimer. The functional role of the glycine-hinge in chemoreceptor signaling has been a topic of much speculation and is somewhat controversial. Mutational analyses have shown that sidechain replacements at the glycine hinge residues impair or abrogate chemotaxis ability (22, 47). Moreover, several studies have suggested that the glycine hinge may introduce structural flexibility to the helix bundle, perhaps to allow bending (14, 22). However, previous MD simulations suggested that the glycine hinge did not show a particularly high propensity to bend in receptors out of the array context (31, 48).

A recent cryo-EM study of Tar dimers inserted in nanodiscs showed that receptors bent in two areas under these conditions: just below the HAMP domain and around the glycine hinge (23). That study proposed that bending at the glycine hinge was not related to output state, but instead crucial for facilitating receptor clustering without structural clashes. Yet, that study lacked the structural context of extended arrays, where interactions with CheA and CheW might have substantial effects on receptor structure. Our data indicate that the glycine hinge probably plays a crucial role in facilitating the dimer zipping motions required to mediate the conformational shift between kinase-ON and kinase-OFF output states. Bending at the glycine hinge might, for

example, serve to structurally couple changes in helix packing of the MH bundle to signaling changes at the receptor hairpin tip. Further improvements in cryo-EM maps to sub-nanometer resolution should elucidate the mechanism of signal propagation through the glycine hinge.

Stability of the receptor tip in different signaling states

The "yin-yang" hypothesis proposed that dynamic motions of the MH bundle and the protein interaction region at the receptor's hairpin tip are coupled in opposition (30). Thus, this model predicts that receptor tips might be "frozen" in the OFF state and relatively "molten" in the ON state. Given that the Tsr protein interaction regions appeared quite similar in our kinase-ON and kinase-OFF maps, our ECT data do not support a large dynamic structural difference between the two output states. The tip bundle contains multiple interaction surfaces that maintain the structural integrity of the trimers and the core units. Thus, it seems likely that the tip adopts alternative, stable conformations in both signaling states through structural changes that are small in magnitude. MD simulations of a Tsr dimer proposed a conformational switch at the receptor tip through state-dependent flips in phenylalanine stacking (31). Symmetric rotations of the dimers about the trimer axis could produce those conformational changes at both the Tsr•P5 and Tsr•CheW interfaces (25). Taking these considerations into account, it is plausible that dimer zipping may promote a reversible twisting motion of receptors at the tip region that triggers a discrete conformational switching between signaling output states.

Effects of receptor signaling state on the kinase

Receptor signaling state influences the mobility of the CheA P1 and P2 domains in core complexes (34). Our data support this conclusion because we found that CheA had a larger keel

volume in the kinase-OFF state. In addition, we observed dimer zipping in the baseplate region of receptors in kinase-OFF signaling complexes. Thus, it is plausible that conformational coupling between zipped receptors "freezes" their tightly packed hairpin tips and CheA domains in the kinase-OFF conformational state. In the kinase-ON state, the CheA keel (domains P1, P2 and possibly P4) is less prominent, consistent with a broader range of domain motions. However, we saw no evidence for enhanced mobility of the receptor tips in kinase-ON signaling complexes. We suggest, therefore, that in the kinase-ON state, receptor tips adopt a discrete, structurally stable conformation that frees up CheA domain motions to promote the autophosphorylation reaction. CheA control probably occurs through the receptor/CheW and CheW/CheA.P5 interfaces (25, 32, 33), in turn modulating the CheA•P4 domain (49-51) and possibly the CheA P3/P3' dimer interface (52).

Our data show that the AW dimer undergoes a change in rigidity between the kinase-ON and OFF state. Asymmetric signaling within receptor trimers has been previously suggested based on the observation that only one dimer within a receptor trimer conveys ligand-binding information to CheA (52). Our results suggest that conformational changes caused by adaptational modification of individual dimers manifest themselves at the level of receptor trimers to modulate kinase control. Thus, although receptor dimers within a trimer undergo asymmetric conformational dynamics depending on their position within signaling complexes, all three dimers play a role in conveying signals to the kinase.

Summary

Despite considerable effort, a complete understanding of the signal transduction events occurring between ligand binding and the regulation of CheA autophosphorylation is still lacking. This can be attributed to the structural complexity of the intact array system, together with the difficulty of analyzing signal transduction events in this context. Our study reveals the conformation dynamics of the *E. coli* Tsr in its native structural context, highlighting global changes in receptor conformation in different signaling states. Our new observations surrounding (1) stability changes in methylation helix bundle, (2) zipping in flexible bundle region, and (3) asymmetric rigidity changes at the receptor tips collectively reflect that the conformational changes corresponding to signaling states takes place in the whole kinase control module of the receptor rather than a single region. Altogether, our results provide crucial insights into the structural and functional changes in the receptors in the context of native arrays.

Materials and Methods

E. coli strains

E. coli strains used in this study are derivatives of RP437, a wild-type chemotaxis derivative of *E. coli* K12 (53) . The strains were previously described (34), which were further modified by introducing a flgM deletion to enhance expression of class III flagellar and chemotaxis genes (Table S1).

383 ***E. coli* cell lysis and cryo specimen preparation**

384 *E. coli* strains were cultured in Tryptone Broth at 30°C with 200 rpm shaking overnight. An
385 overnight culture of *E. coli* was diluted into 50 ml at 1:100 ratio. The diluted culture was then
386 allowed to grow till its OD600 reached 0.2. Then, Penicillin G potassium salt (Carl Ruth,
387 Karlsruhe, Germany) was added to the culture for a working concentration of 2000 UI/ml. After
388 30 minutes of incubation at 30 degrees, the cells from 1ml culture were collected by
389 centrifugation at 13000 rpm in a 1.5 ml Eppendorf tube. The supernatant was discarded, pellets
390 were resuspended in 10 µl PBS buffer and kept on ice.
391 The protein A - treated 10nm colloidal gold solution (Cell Microscopy Core, Utrecht University,
392 Utrecht, The Netherlands) was mixed with penicillin treated cells at a 1:10 ratio. After brief
393 vortexing, an aliquot of 3 µl mixture was applied to a freshly plasma-cleaned R2/2, 200mesh
394 copper Quantifoil grids (Quantifoil Micro Tools GmbH, Jena, Germany) and applied to the EM
395 grid in the climate chamber of a Leica EMGP (Leica microsystems, Wetzlar, Germany). The
396 grid was blotted for 1 second from the carbon-facing side of the grid at room temperature (20°C)
397 and 95% humidity. Plunge freeing was carried out in liquid ethane at – 183 °C. Grids were
398 stored in liquid nitrogen until data acquisition.
399

400 **Cryo-electron tomography**

401 Data acquisition was performed on a Titan Krios transmission electron microscope (Thermo
402 Fisher Scientific (formerly FEI, Hillsboro, OR, USA) operating at 300 kV. Images were
403 recorded with a Gatan K2 Summit direct electron detector (Gatan, Pleasanton, CA) equipped
404 with a GIF-quantum energy filter (Gatan, Pleasanton, CA) operating with a slit width of 20eV.
405 Images were taken at a nominal magnification of 42,000 x, which corresponded to a pixel size of

3.5Å. The UCSFtomo software package was used for data acquisition with low-dose mode and dose fractionation within a cumulative exposure of 80 e-/A^2 (54) . All tilt series were collected using a bidirectional tilt scheme which started from 0° to −60° and continued from 0° to 60° tilting with a 2° increment. Defocus was set to -8 μm. A total of 28 tilt series were collected for each strain.

Tomogram reconstruction and subtomogram averaging

IMOD software was used for drift correction and bead-tracking based tilt series alignment (55, 56). CTF estimation and correction were done with CTFPLOTTER and CTFPHASEFLIP implemented in IMOD (57). Tomograms was reconstructed for each tilt series by weighted back projection, both with and without SIRT-like filter equivalent to 9 SIRT iterations. Tomograms reconstructed with the SIRT-like filter provided strong contrast for evaluating array distribution and particle picking and initial template building; while tomograms built by weighted backprojection was used for subtomogram extraction, alignment and averaging.

Subtomogram averaging was done with the Dynamo software package (58-60). The initial subtomograms were defined as six trimmers of receptor dimers packed in hexagonal order. Subtomograms were manually picked from selected tomograms binned by 2. After coarse alignment based largely on the receptor hexagons, principal component analysis and k-mean based classification was performed based on the CheA occupancy beneath the receptor hexagon. Subtomograms were extracted from tomograms reconstructed by SIRT-like weighted backprojection, since they provided strong contrast for receptor hexagon alignment and CheA-based classification. Each CheA filled hexagon consists of three signaling core units following

C3 symmetry. Sub-boxing was carried out to extract the individual core units for further alignment. In addition, an extra round of sub-boxing was done to extract two receptor trimers of dimers from each core unit. For trimer alignment, a soft cylindrical mask was applied to enclose the trimer density. All final maps were calculated from weighted back-projection tomograms. The Fourier shell correlation curves for the core unit maps were calculated with the EMAN2 software package (61). Surface visualization was done using the Chimera software package (62-64). The particle numbers used of averages are listed in supplementary materials (Table S2).

Model building

A preliminary model of the Tsr trimer-of-dimers was constructed by aligning a copy of PDB 3ZX6 (42), which contains the complete cytoplasmic anti-parallel coiled-coil domain of Tsr (residues 259-516), with the protein-interaction region of each partial homodimer seen in the crystal structure of Tsr trimer of dimers (PDB 1QU7, residues 340-440). Using VMD, the model was then hydrated with TIP3P water molecules and subsequently neutralized and ionized with potassium and chloride ions to a concentration of 150 mM, resulting in a system containing 239,688 atoms. The complete system was then subjected to an energy minimization followed by a 50 ns equilibration simulation in which the protein backbone was harmonically constrained. Targeted Molecular Dynamics was then used to reproduce the inter-homodimer interfaces seen in PDB 1QU7 by minimizing the root-mean-squared-deviation between the backbone and side chain positions in the protein interaction region of the two structures. The resulting model was used as the input structure for subsequent MDFF simulations.

Molecular dynamics simulations

All molecular dynamics simulations were carried out using NAMD 2.12 (65) and the CHARMM36 force field (66). MDFF simulations were performed in the NVT ensemble at 310 K for 20 ns. A scaling factor of 0.15 was used to couple backbone atoms to the MDFF potential. Additional harmonic restraints were applied during fitting to prevent loss of secondary structure. Isothermal conditions were maintained by a Langevin thermostat. The r-RESPA integrator scheme with an integration time step of 2 fs was used along with SHAKE constraints on all hydrogen atoms. Short-range, non-bonded interactions were calculated every 2 fs with a cutoff of 12 Å while long-range electrostatics were evaluated every 6 fs using the particle-mesh-Ewald (PME) method with a grid size of 1 Å.

Accession numbers

The EMDB accession numbers for the subtomogram averages of signaling core unit in different kinase activation level reported in this study are: EMD_4991 (Tsr_EEEE); EMD_4992 (Tsr_QQQQ) and EMD_4993 (Tsr_QEQE).

Acknowledgements

This work was supported by the US National Science Foundation grant PHY1430124 (Z.L.-S.), the US National Institutes of Health grant P41-GM104601 (Z.L.-S.), the UK Biotechnology and Biological Sciences Research Council grant BB/S003339/1 (C.K.C), and the US National Institute of General Medical Sciences grant GM19559 (J.S.P). The Protein-DNA Core Facility at the University of Utah receives support from National Cancer Institute grant CA42014 to the Huntsman Cancer Institute. This research made use of the Blue Waters supercomputer, which is supported by the National Science Foundation (OCI-0725070 and ACI-1238993) and the state of

Illinois. This work is part of the Petascale Computational Resource grant, which is supported by the NSF (ACI-1713784).

References

1. Parkinson JS, Hazelbauer GL, Falke JJ. 2015. Signaling and sensory adaptation in Escherichia coli chemoreceptors: 2015 update. Trends Microbiol 23:257-66.
2. Falke JJ, Piasta KN. 2014. Architecture and signal transduction mechanism of the bacterial chemosensory array: progress, controversies, and challenges. Curr Opin Struct Biol 29:85-94.
3. Hazelbauer GL, Falke JJ, Parkinson JS. 2008. Bacterial chemoreceptors: high-performance signaling in networked arrays. Trends Biochem Sci 33:9-19.
4. Frank V, Pinas GE, Cohen H, Parkinson JS, Vaknin A. 2016. Networked Chemoreceptors Benefit Bacterial Chemotaxis Performance. MBio 7.
5. Pinas GE, Frank V, Vaknin A, Parkinson JS. 2016. The source of high signal cooperativity in bacterial chemosensory arrays. Proc Natl Acad Sci U S A 113:3335-40.
6. Borkovich KA, Simon MI. 1990. The dynamics of protein phosphorylation in bacterial chemotaxis. Cell 63:1339-48.

496 7. Sourjik V, Wingreen NS. 2012. Responding to chemical gradients: bacterial chemotaxis.
497 Current Opinion in Cell Biology 24:262-268.
498 8. Ames P, Studdert CA, Reiser RH, Parkinson JS. 2002. Collaborative signaling by mixed
499 chemoreceptor teams in Escherichia coli. Proc Natl Acad Sci U S A 99:7060-5.
500 9. Studdert CA, Parkinson JS. 2004. Crosslinking snapshots of bacterial chemoreceptor
501 squads. Proc Natl Acad Sci U S A 101:2117-22.
502 10. Li M, Hazelbauer GL. 2011. Core unit of chemotaxis signaling complexes. Proc Natl
503 Acad Sci U S A 108:9390-5.
504 11. Briegel A, Li X, Bilwes AM, Hughes KT, Jensen GJ, Crane BR. 2012. Bacterial
505 chemoreceptor arrays are hexagonally packed trimers of receptor dimers networked by
506 rings of kinase and coupling proteins. Proc Natl Acad Sci U S A 109:3766-71.
507 12. Liu J, Hu B, Morado DR, Jani S, Manson MD, Margolin W. 2012. Molecular architecture
508 of chemoreceptor arrays revealed by cryoelectron tomography of Escherichia coli
509 minicells. Proc Natl Acad Sci U S A 109:E1481-8.
510 13. Briegel A, Wong ML, Hodges HL, Oikonomou CM, Piasta KN, Harris MJ, Fowler DJ,
511 Thompson LK, Falke JJ, Kiessling LL, Jensen GJ. 2014. New insights into bacterial
512 chemoreceptor array structure and assembly from electron cryotomography.
513 Biochemistry 53:1575-85.
514 14. Alexander RP, Zhulin IB. 2007. Evolutionary genomics reveals conserved structural
515 determinants of signaling and adaptation in microbial chemoreceptors. Proc Natl Acad
516 Sci U S A 104:2885-90.
517 15. Sourjik V, Berg HC. 2004. Functional interactions between receptors in bacterial
518 chemotaxis. Nature 428:437-441.

16. Herrera Seitz MK, Frank V, Massazza DA, Vaknin A, Studdert CA. 2014. Bacterial chemoreceptors of different length classes signal independently. Mol Microbiol 93:814-22.
17. Kim KK, Yokota H, Kim SH. 1999. Four-helical-bundle structure of the cytoplasmic domain of a serine chemotaxis receptor. Nature 400:787-92.
18. Kitanovic S, Ames P, Parkinson JS. 2015. A Trigger Residue for Transmembrane Signaling in the Escherichia coli Serine Chemoreceptor. J Bacteriol 197:2568-79.
19. Kitanovic S, Ames P, Parkinson JS. 2011. Mutational analysis of the control cable that mediates transmembrane signaling in the Escherichia coli serine chemoreceptor. J Bacteriol 193:5062-72.
20. Parkinson JS. 2010. Signaling mechanisms of HAMP domains in chemoreceptors and sensor kinases. Annu Rev Microbiol 64:101-22.
21. Ames P, Zhou Q, Parkinson JS. 2014. HAMP domain structural determinants for signalling and sensory adaptation in Tsr, the Escherichia coli serine chemoreceptor. Mol Microbiol 91:875-86.
22. Coleman MD, Bass RB, Mehan RS, Falke JJ. 2005. Conserved glycine residues in the cytoplasmic domain of the aspartate receptor play essential roles in kinase coupling and on-off switching. Biochemistry 44:7687-7695.
23. Akkaladevi N, Bunyak F, Stalla D, White TA, Hazelbauer GL. 2018. Flexible Hinges in Bacterial Chemoreceptors. Journal of Bacteriology 200.
24. Piasta KN, Ulliman CJ, Slivka PF, Crane BR, Falke JJ. 2013. Defining a key receptor-CheA kinase contact and elucidating its function in the membrane-bound bacterial

chemosensory array: a disulfide mapping and TAM-IDS Study. Biochemistry 52:3866-80.

25. Pedetta A, Parkinson JS, Studdert CA. 2014. Signalling-dependent interactions between the kinase-coupling protein CheW and chemoreceptors in living cells. Mol Microbiol 93:1144-55.

26. Vu A, Wang XQ, Zhou HJ, Dahlquist FW. 2012. The Receptor-CheW Binding Interface in Bacterial Chemotaxis. Journal of Molecular Biology 415:759-767.

27. Pollard AM, Bilwes AM, Crane BR. 2009. The Structure of a Soluble Chemoreceptor Suggests a Mechanism for Propagating Conformational Signals. Biochemistry 48:1936-1944.

28. Zhou Q, Ames P, Parkinson JS. 2011. Biphasic control logic of HAMP domain signalling in the Escherichia coli serine chemoreceptor. Mol Microbiol 80:596-611.

29. Zhou Q, Ames P, Parkinson JS. 2009. Mutational analyses of HAMP helices suggest a dynamic bundle model of input-output signalling in chemoreceptors. Mol Microbiol 73:801-14.

30. Swain KE, Gonzalez MA, Falke JJ. 2009. Engineered socket study of signaling through a four-helix bundle: evidence for a yin-yang mechanism in the kinase control module of the aspartate receptor. Biochemistry 48:9266-77.

31. Ortega DR, Yang C, Ames P, Baudry J, Parkinson JS, Zhulin IB. 2013. A phenylalanine rotameric switch for signal-state control in bacterial chemoreceptors. Nat Commun 4:2881.

32. Natale AM, Duplantis JL, Piasta KN, Falke JJ. 2013. Structure, function, and on-off switching of a core unit contact between CheA kinase and CheW adaptor protein in the

564 bacterial chemosensory array: A disulfide mapping and mutagenesis study. Biochemistry
565 52:7753-65.
566 33. Pinas GE, DeSantis MD, Parkinson JS. 2018. Noncritical Signaling Role of a Kinase-
567 Receptor Interaction Surface in the Escherichia coli Chemosensory Core Complex. J Mol
568 Biol 430:1051-1064.
569 34. Briegel A, Ames P, Gumbart JC, Oikonomou CM, Parkinson JS, Jensen GJ. 2013. The
570 mobility of two kinase domains in the Escherichia coli chemoreceptor array varies with
571 signalling state. Mol Microbiol 89:831-41.
572 35. Erbse AH, Falke JJ. 2009. The core signaling proteins of bacterial chemotaxis assemble
573 to form an ultrastable complex. Biochemistry 48:6975-87.
574 36. Slivka PF, Falke JJ. 2012. Isolated bacterial chemosensory array possesses quasi- and
575 ultrastable components: functional links between array stability, cooperativity, and order.
576 Biochemistry 51:10218-28.
577 37. Fu X, Himes BA, Ke D, Rice WJ, Ning J, Zhang P. 2014. Controlled bacterial lysis for
578 electron tomography of native cell membranes. Structure 22:1875-82.
579 38. Chevance FFV, Hughes KT. 2008. Coordinating assembly of a bacterial macromolecular
580 machine. Nature Reviews Microbiology 6:455-465.
581 39. Briegel A, Pilhofer M, Mastronarde DN, Jensen GJ. 2013. The challenge of determining
582 handedness in electron tomography and the use of DNA origami gold nanoparticle
583 helices as molecular standards. J Struct Biol 183:95-8.
584 40. Greenswag AR, Li X, Borbat PP, Samanta D, Watts KJ, Freed JH, Crane BR. 2015.
585 Preformed Soluble Chemoreceptor Trimers That Mimic Cellular Assembly States and
586 Activate CheA Autophosphorylation. Biochemistry 54:3454-68.

587 41. Cassidy CK, Himes BA, Alvarez FJ, Ma J, Zhao G, Perilla JR, Schulten K, Zhang P.
588 2015. CryoEM and computer simulations reveal a novel kinase conformational switch in
589 bacterial chemotaxis signaling. Elife 4.
590 42. Ferris HU, Zeth K, Hulko M, Dunin-Horkawicz S, Lupas AN. 2014. Axial helix rotation
591 as a mechanism for signal regulation inferred from the crystallographic analysis of the E.
592 coli serine chemoreceptor. Journal of Structural Biology 186:349-356.
593 43. McGreevy R, Teo I, Singharoy A, Schulten K. 2016. Advances in the molecular
594 dynamics flexible fitting method for cryo-EM modeling. Methods 100:50-60.
595 44. Cassidy CK, Himes BA, Luthey-Schulten Z, Zhang P. 2018. CryoEM-based hybrid
596 modeling approaches for structure determination. Curr Opin Microbiol 43:14-23.
597 45. Strelkov SV, Burkhard P. 2002. Analysis of alpha-helical coiled coils with the program
598 TWISTER reveals a structural mechanism for stutter compensation. J Struct Biol 137:54-
599 64.
600 46. Starrett DJ, Falke JJ. 2005. Adaptation mechanism of the aspartate receptor: electrostatics
601 of the adaptation subdomain play a key role in modulating kinase activity. Biochemistry
602 44:1550-60.
603 47. Pedetta A, Massazza DA, Herrera Seitz MK, Studdert CA. 2017. Mutational
604 Replacements at the "Glycine Hinge" of the Escherichia coli Chemoreceptor Tsr Support
605 a Signaling Role for the C-Helix Residue. Biochemistry 56:3850-3862.
606 48. Hall BA, Armitage JP, Sansom MS. 2012. Mechanism of bacterial signal transduction
607 revealed by molecular dynamics of Tsr dimers and trimers of dimers in lipid vesicles.
608 PLoS Comput Biol 8:e1002685.

609 49. Wang X, Wu C, Vu A, Shea JE, Dahlquist FW. 2012. Computational and experimental
610 analyses reveal the essential roles of interdomain linkers in the biological function of
611 chemotaxis histidine kinase CheA. J Am Chem Soc 134:16107-10.
612 50. Wang XQ, Vallurupalli P, Vu A, Lee K, Sun S, Bai WJ, Wu C, Zhou HJ, Shea JE, Kay
613 LE, Dahlquist FW. 2014. The Linker between the Dimerization and Catalytic Domains of
614 the CheA Histidine Kinase Propagates Changes in Structure and Dynamics That Are
615 Important for Enzymatic Activity. Biochemistry 53:855-861.
616 51. Ding XY, He Q, Shen FL, Dahlquist FW, Wang XQ. 2018. Regulatory Role of an
617 Interdomain Linker in the Bacterial Chemotaxis Histidine Kinase CheA. Journal of
618 Bacteriology 200.
619 52. Li M, Hazelbauer GL. 2014. Selective allosteric coupling in core chemotaxis signaling
620 complexes. Proc Natl Acad Sci U S A 111:15940-5.
621 53. Parkinson JS, Houts SE. 1982. Isolation and behavior of Escherichia coli deletion
622 mutants lacking chemotaxis functions. J Bacteriol 151:106-13.
623 54. Zheng SQ, Keszthelyi B, Branlund E, Lyle JM, Braunfeld MB, Sedat JW, Agard DA.
624 2007. UCSF tomography: an integrated software suite for real-time electron microscopic
625 tomographic data collection, alignment, and reconstruction. J Struct Biol 157:138-47.
626 55. Kremer JR, Mastronarde DN, McIntosh JR. 1996. Computer Visualization of Three-
627 Dimensional Image Data Using IMOD. Journal of Structural Biology 116:71-76.
628 56. Mastronarde DN. 2008. Correction for non-perpendicularity of beam and tilt axis in
629 tomographic reconstructions with the IMOD package. J Microsc 230:212-7.

57. Xiong Q, Morphew MK, Schwartz CL, Hoenger AH, Mastronarde DN. 2009. CTF determination and correction for low dose tomographic tilt series. J Struct Biol 168:378-87.

58. Castano-Diez D. 2017. The Dynamo package for tomography and subtomogram averaging: components for MATLAB, GPU computing and EC2 Amazon Web Services. Acta Crystallogr D Struct Biol 73:478-487.

59. Castano-Diez D, Kudryashev M, Stahlberg H. 2017. Dynamo Catalogue: Geometrical tools and data management for particle picking in subtomogram averaging of cryo-electron tomograms. J Struct Biol 197:135-144.

60. Castano-Diez D, Kudryashev M, Arheit M, Stahlberg H. 2012. Dynamo: a flexible, user-friendly development tool for subtomogram averaging of cryo-EM data in high-performance computing environments. J Struct Biol 178:139-51.

61. Tang G, Peng L, Baldwin PR, Mann DS, Jiang W, Rees I, Ludtke SJ. 2007. EMAN2: An extensible image processing suite for electron microscopy. Journal of Structural Biology 157:38-46.

62. Goddard TD, Huang CC, Ferrin TE. 2007. Visualizing density maps with UCSF Chimera. Journal of Structural Biology 157:281-287.

63. Goddard TD, Huang CC, Ferrin TE. 2005. Software extensions to UCSF Chimera for interactive visualization of large molecular assemblies. Structure 13:473-482.

64. Pettersen EF, Goddard TD, Huang CC, Couch GS, Greenblatt DM, Meng EC, Ferrin TE. 2004. UCSF Chimera--a visualization system for exploratory research and analysis. J Comput Chem 25:1605-12.

652 65. Phillips JC, Braun R, Wang W, Gumbart J, Tajkhorshid E, Villa E, Chipot C, Skeel RD,
653 Kale L, Schulten K. 2005. Scalable molecular dynamics with NAMD. J Comput Chem
654 26:1781-802.
655 66. Huang J, MacKerell AD, Jr. 2013. CHARMM36 all-atom additive protein force field:
656 validation based on comparison to NMR data. J Comput Chem 34:2135-45.
657 67. Han XS, Parkinson JS. 2014. An unorthodox sensory adaptation site in the Escherichia
658 coli serine chemoreceptor. J Bacteriol 196:641-9.
659 68. Tajima H, Imada K, Sakuma M, Hattori F, Nara T, Kamo N, Homma M, Kawagishi I.
660 2011. Ligand specificity determined by differentially arranged common ligand-binding
661 residues in bacterial amino acid chemoreceptors Tsr and Tar. J Biol Chem 286:42200-10.

662

663 **Figures**

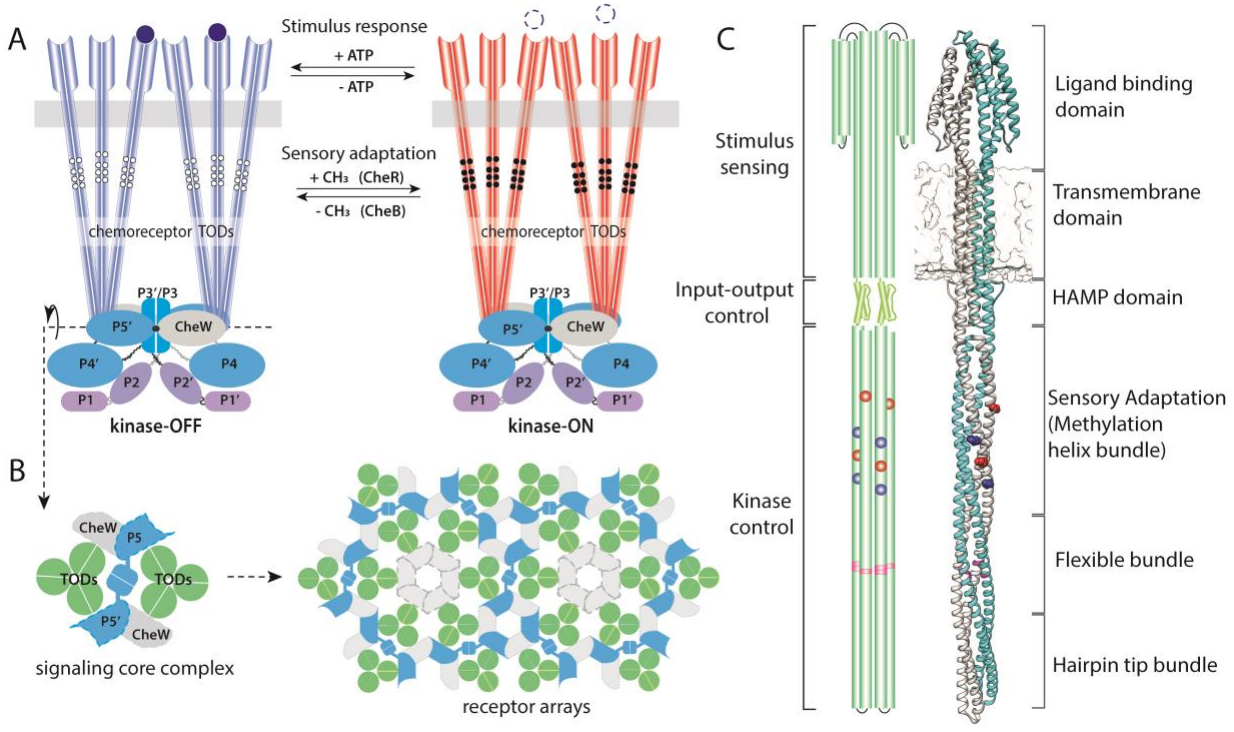

664

Figure 1. Functional architecture of the *E. coli* chemoreceptor array and the Tsr receptor. (A) A two-state model of receptor signaling in the core complex, viewed from the side with the cytoplasmic membrane (gray rectangle) near the top. The CheA homodimer and two molecules of CheW bind to the hairpin tips of two receptor trimers. The five CheA domains are designated P1-P5 in one subunit and P1'-P5' in the other. White and black circles indicate the modification states of the receptor methylation sites in the kinase-off (white circles, EEEE sites) and kinase-on (black circles, QQQQ sites) output states. (B) A top-down cross-section through the protein interaction region of the signaling core unit. Core units assemble into an extended receptor array through hexagonal, six membered P5-CheW and CheW-CheW rings. (C) Cartoon and atomic model of the *E. coli* serine receptor (Tsr). The Tsr homodimer consists mainly of alpha-helical segments (cylinders, drawn approximately to scale) organized in four-helix bundles. Four methylation sites are indicated in each subunit, with red indicating glytamyl residues (E493 & E304) and blue glutaminyl residues (Q297 & Q311) in the wild-type receptor. A fifth Tsr methylation site (E502) is not shown or discussed in the text because it is less critical for sensory adaptation (67). Glycine residues (G340, G341 and G439) located in the middle of the flexible bundle comprise the glycine hinge (highlighted in magenta). Atomic model of the full length Tsr is built based on the structure of HAMP-Tsr fusion (PDB 3ZX6) and the ligand binding domain of Tsr (PDB 3ATP) (42, 68).

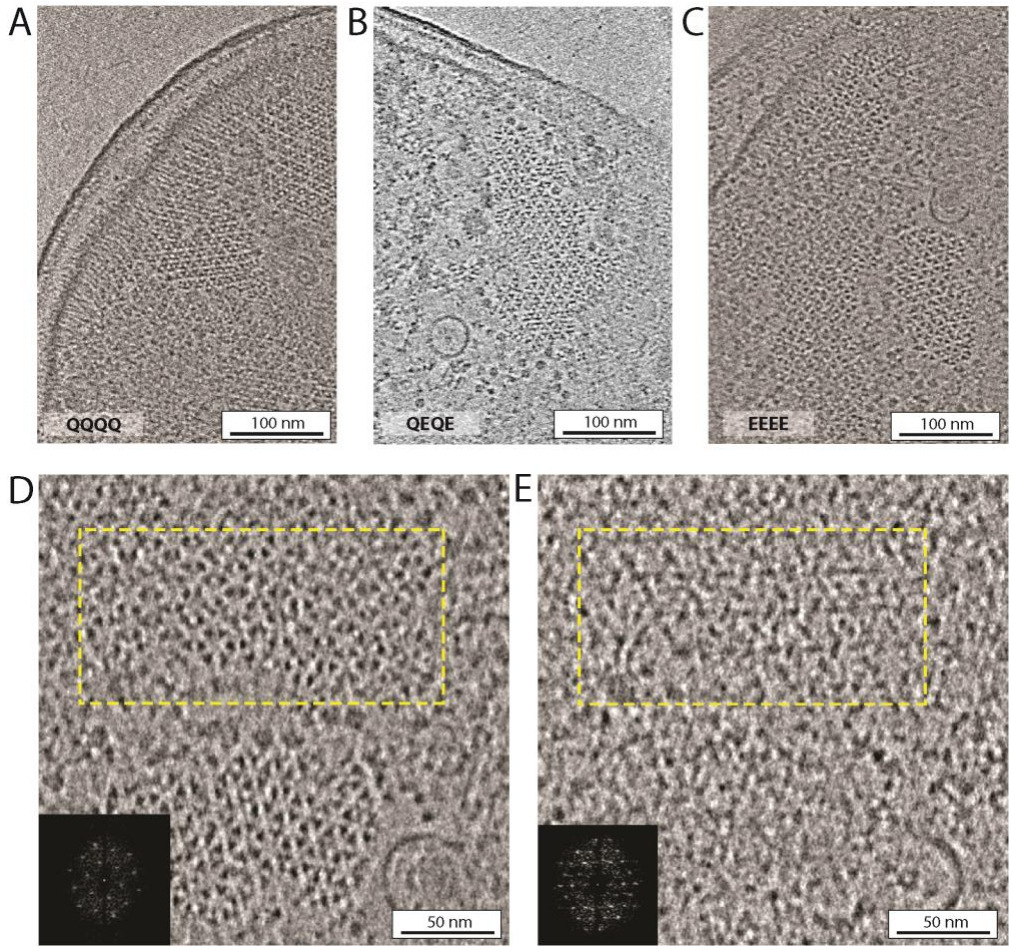

Figure 2. Chemoreceptor arrays imaged by cryo-ET of lysed cells. Panels show 10 nm tomoslices near the cell pole. (A) Tsr-QQQQ (B)Tsr-QEQE (C) Tsr- EEEE. (D) Magnified area of a Tsr-EEEE array (E) Magnified region located 14 nm beneath the array of panel C, showing the ordered CheA distribution in the baseplate. Insets are the power spectra of the regions highlighted by the yellow dashed line in both panels (not to scale). The circular structures in panels B-E are the C-ring of a flagellar motor.

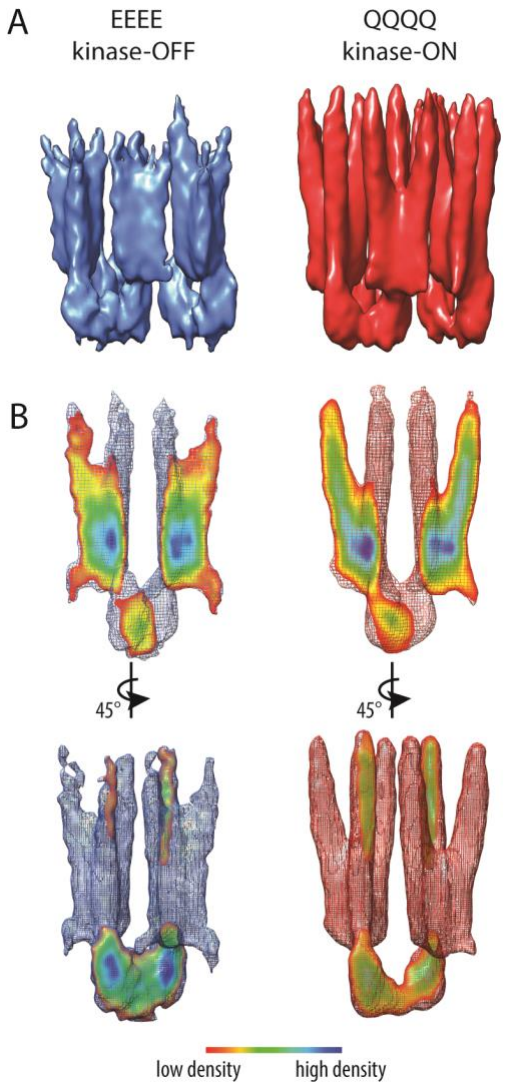

692

693 Figure 3. Subtomogram averaging results for Tsr-EEEE and Tsr-QQQQ arrays (A)

694 Subtomogram average of hexagonal structural units (six Tsr trimers and three CheA dimers). (B)

695 Density maps of chemoreceptor core complexes showing a cross-section through the receptor

696 trimers and the CheA dimer. Mesh surfaces are contoured at 1.5 σ. Cross-section colors indicate

697 the volume density. Red corresponds to a low density value, blue to a high density value.

698

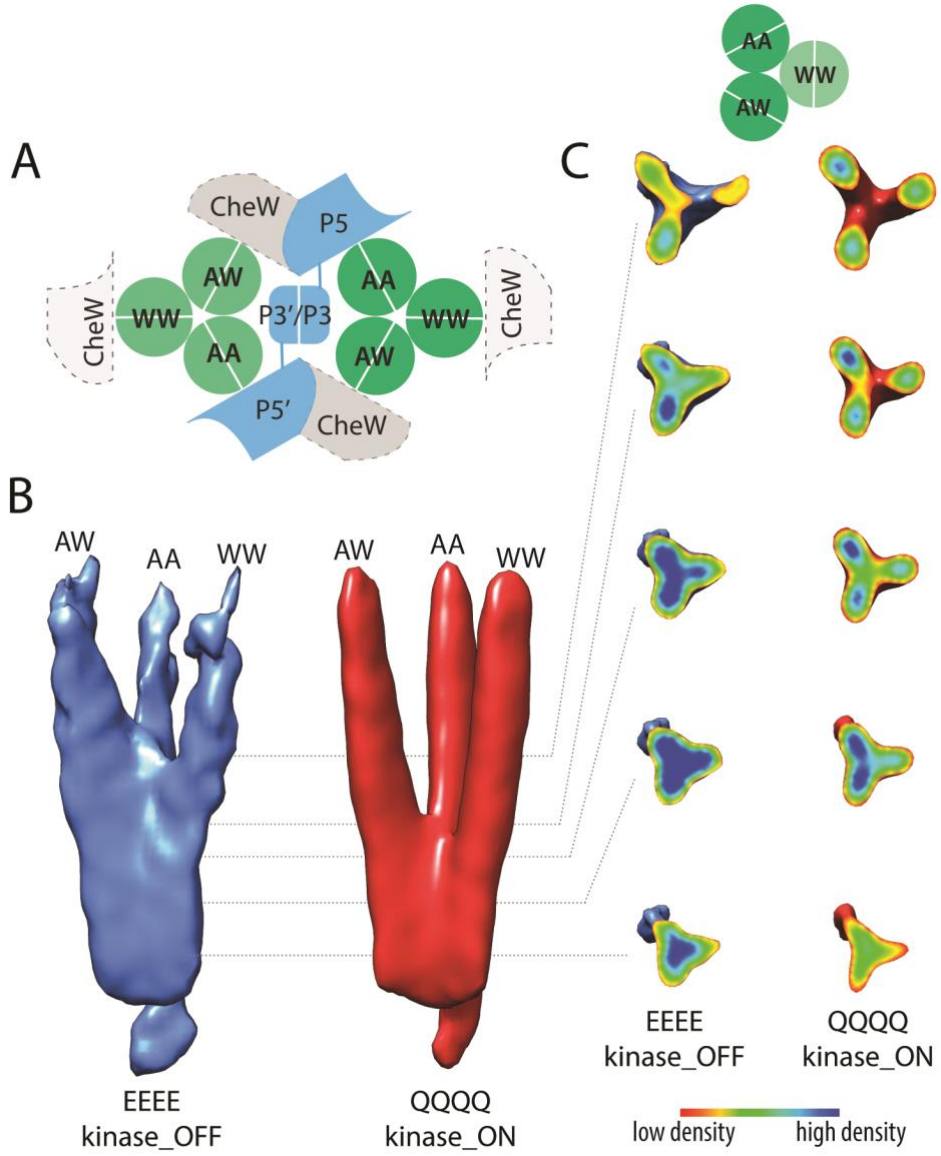

699

700 Figure 4. Tsr trimers in different output states. (A) Nomenclature for the three members of a
701 receptor trimer in the signaling core unit. Each Tsr dimer contacts different baseplate
702 components. WW dimers may bind to CheW rings in the array, but are shown in light gray with
703 dashed outlines because their extent of CheW occupancy has not yet been established. (B)
704 Density distribution of the receptor trimer of dimers in kinase-ON and kinase-OFF output states.
705 In both states, the AA and AW dimers exhibit a greater coherence compared to the WW dimer,
706 which exhibited the lowest stability in both maps. (C) The density distribution in different cross-

707 sections of the trimer along the trimer axis, using a color scale from red (low density) to blue
708 (high density).
709

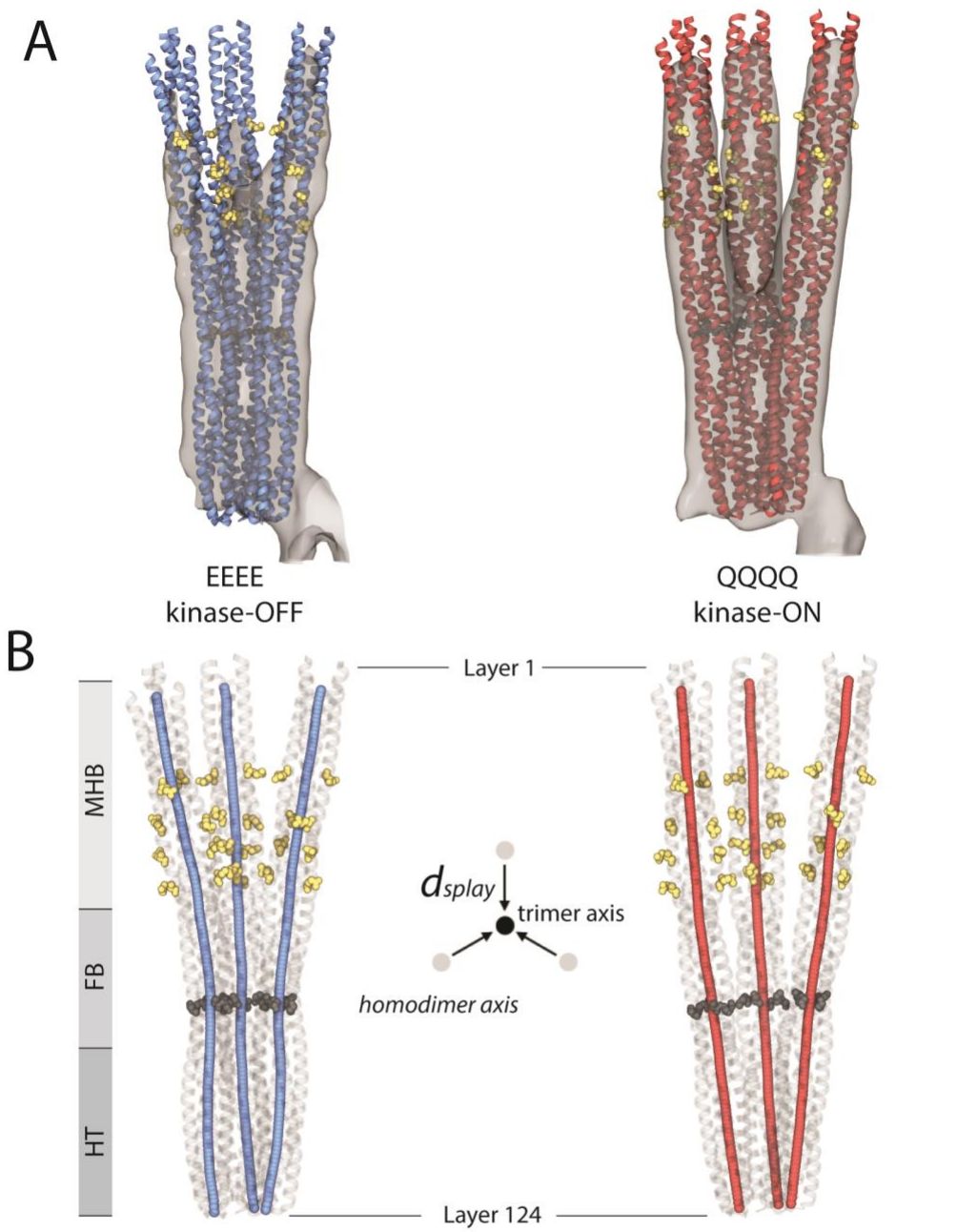
A
EEEE
kinase-OFF
QQQQ
kinase-ON
B
Layer 1
MHB
FB
HT
d_{splay}
trimer axis
homodimer axis
Layer 124
C
MHB
FB
HT
AA
AW
WW
d_{splay} (Å)
Coiled Coil Layer

Figure 5. Signal-state differences in trimer compactness. (A) Overlays of the EEEE and QQQQ density maps and representative MDFF-derived Tsr backbone configurations. (B) Central axes of the homodimers in each trimer conformation. Receptor regions are the methylation helix bundle (MHB) and modification sites (yellow atoms), the flexible bundle (FB) and glycine hinge (dark gray atoms) and the hairpin tip (HT). (C) Plots of the distance between the central axis of each homodimer and the symmetry axis of the trimer (d_{splay}). Gray dashed lines denote coiled-coil layers containing the glycine hinge; black dashed lines denote layers containing methylation sites.

Supplementary Figures

Strains	Relevant genotype	Ref
UU2981	(flgM)Δ494 tsr-QQQQE (tar-cheB)Δ4346Δaer1(trg)Δ4543	This work
UU2982	(flgM)Δ494 (tar-cheB)Δ4346 Δaer-1(trg)Δ4543	This work
UU2983	flgM)Δ494 tsr-EEEEE (tar-cheB)Δ4346 Δaer-1(trg)Δ4543	This work

722

723 Supplementary table 1. *E.coli* strains used in this study.

724

	Tsr_QQQQ	Tsr_QEQE	Tsr_EEEE
Receptor hexagon	1251	1011	1118
Signaling core unit	1977	2813	3148
Receptor trimer	3613	5686	6017

Supplementary table 2. The particle numbers for calculating the subtomogram averaging results for the Tsr receptor hexagons with triple CheAs, the signaling core unit and the Tsr trimers.

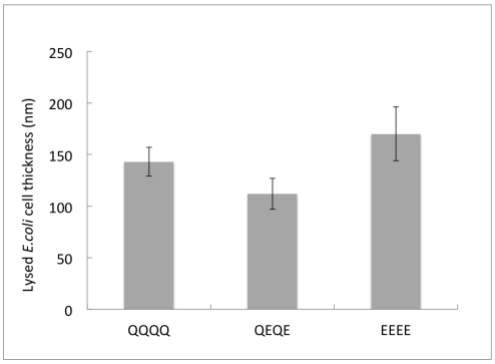

729

730 Supplementary figure 1. The average lysed *E.coli* cell thickness measured from the tomographic
731 date of samples that contained chemoreceptor array. Although in total 30 tomograms were
732 collected for each strain, chemoreceptor complexes for subtomogram averaging were picked
733 from 11, 8 and 7 tomograms for strains expressing Tsr_QQQQ, Tsr_QEQE and Tsr_EEEE,
734 respectively. Student T test ($P<0.05$) states that cells solely expressing Tsr_QQQQ and
735 Tsr_EEEE are of similar cells thickness after lysed, while cells expressing Tsr_QEQE was on
736 average thinner compared to other groups.

737

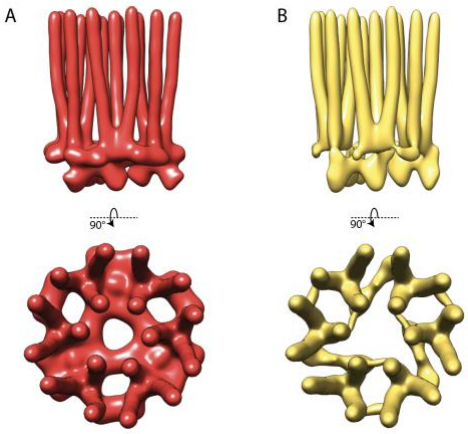

738

739 Supplementary figure 2. Simulation of receptor hexagon maps under impact of a missing cone
740 that corresponds to a -60° to 60° tilt scheme. (A) Density map for the receptor hexagon was built
741 with core compel model (PDF 3JA6). (B) The map of the receptor hexgon with a soft-edged,
742 missing cone shape mask applied in the Fourier space. From both the side and top view, the
743 missing core affect little on the size and shape of the receptor; mainly it causes a severe
744 underrepresentation of the CheWs and a shape distortion in the P4 and P5 domains of CheA.

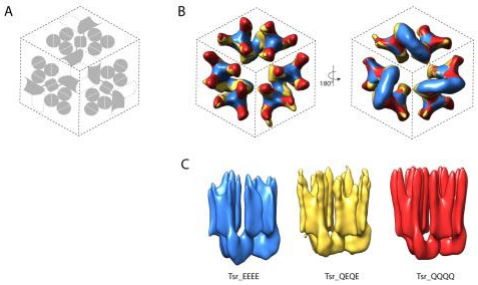

Supplementary figure 3. Subtomogram averaging of receptors hexagon composed with three dimeric CheA and different receptor variants. A. Graphic scheme illustrates the native packing order of the ternary complex in the array lattice, in where each haxegon is consisted of three signaling core units. Components in gray, including the receptor trimers and the CheA, are strongly present in the maps; while the coupling protein CheW in the baseplate (color in white) is not resolve due to a combination of its low molecular weight and the impact from missing cone. B. Overlay of receptor hexagon for strains containing three Tsr receptor variants show the same native packing order. C . Averages for three Tsr variants are each low-pass filtered to the same resolution, 25Å , and present at 1.5σ level.

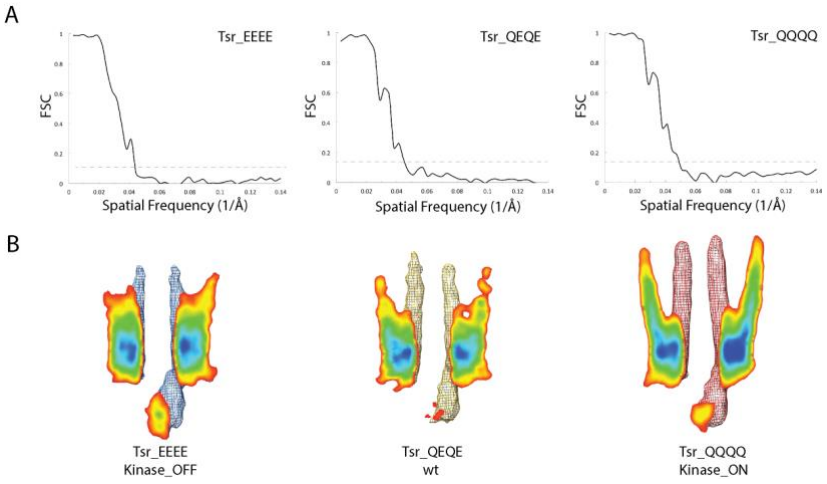
A
Tsr_EEEE
Tsr_QEQE
Tsr_QQQQ
FSC
Spatial Frequency (1/Å)
B
Tsr_EEEE
Kinase_OFF
Tsr_QEQE
wt
Tsr_QQQQ
Kinase_ON

Supplementary figure 4. The Fourier shell correlation (FSC) curves and the map cross-sections of the signaling core unit averaged for all three selected strains. A. The FSC curves are plotted for each signaling core unit calculated for the corresponding strains. The dash lines indicate the cutoff at 0.143. All three maps for core units share similar resolutions, which are 20.1Å , 22.8Å and 23.6Å for Tsr_QQQQ, Tsr_QEQE and Tsr_EEEE, respectively. B. The cross sections of the three maps show the density distribution of the core units. Tsr_QEQE map appears as the intermediate state between the kinase-on and kinase-off biased output states. The surfaces of all maps are rendered at 1.5σ level in mesh, the cross section is colored according to the volume density value, where the red color correspond to a weaker density than the blue.

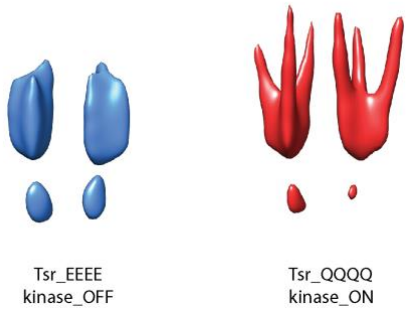

768

769 Supplementary figure 5. The core unit maps for Tsr_EEEE (blue) and Tsr_QQQQ (red) are

770 low-pass filtered to 25 Å and present at 3σ level still show a rigid trimer splay in the kinase-ON

771 state and a zipping in the kinase_OFF state.

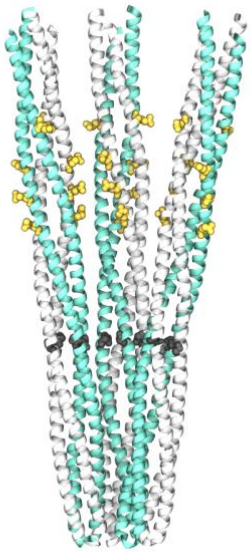

Supplementary figure 6. Atomistic model of the cytoplasmic Tsr trimer-of-dimers (residues 259-516) used in this study. Individual monomers within each homodimer are colored in teal and white. Methylation sites (residues Q297, E304, Q311, E493) and the glycine hinge (residues G340, G431, G439) are shown with a space-filling representation in yellow and dark-grey, respectively.

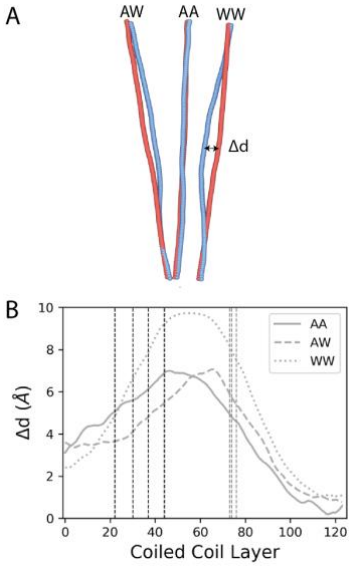

780

781 Supplementary figure 7. (A) Overlay between the central axes of representative EEEE (blue) and

782 QQQQ (red) receptor trimer conformations. The distance (d_{splay}) between each receptor

783 homodimer to the central axe varies for EEEE and QQQQ (Δd). (B) Plot depicting the distance

784 changes (Δd) of the AA, AW, and WW homodimers shown in panel A, which reflects the

785 inhomogeneity of the trimer compactness changes.